

Article

Hollow $g\text{-C}_3\text{N}_4@Cu_{0.5}In_{0.5}S$ Core-Shell S-Scheme Heterojunction Photothermal Nanoreactors with Broad-Spectrum Response and Enhanced Photocatalytic Performance

Yawei Xiao ¹, Zhezhe Wang ¹, Bo Yao ¹, Yunhua Chen ², Ting Chen ^{3,*} and Yude Wang ^{4,*} 

- ¹ National Center for International Research on Photoelectric and Energy Materials, School of Materials and Energy, Yunnan University, Kunming 650504, China; zzwang@mail.ynu.edu.cn (Z.W.); yaobo@mail.ynu.edu.cn (B.Y.)
- ² Department of Physics, Yunnan University, Kunming 650504, China; yhchen@ynu.edu.cn
- ³ Institute of Materials Science & Devices, School of Materials Science and Engineering, Suzhou University of Science and Technology, Suzhou 215009, China
- ⁴ Yunnan Key Laboratory of Carbon Neutrality and Green Low-Carbon Technologies, Yunnan University, Kunming 650504, China
- * Correspondence: chenting@mail.usts.edu.cn (T.C.); ydwang@ynu.edu.cn (Y.W.)

Abstract: Improving spectral utilization and carrier separation efficiency is a key point in photocatalysis research. Herein, we prepare hollow $g\text{-C}_3\text{N}_4$ nanospheres by the template method and synthesize a $g\text{-C}_3\text{N}_4@Cu_{0.5}In_{0.5}S$ core-shell S-scheme photothermal nanoreactor by a simple chemical deposition method. The unique hollow core-shell structure of $g\text{-C}_3\text{N}_4@Cu_{0.5}In_{0.5}S$ is beneficial to expand the spectral absorption range and improving photon utilization. At the same time, the photogenerated carriers can be separated, driven by the internal electric field. In addition, $g\text{-C}_3\text{N}_4@Cu_{0.5}In_{0.5}S$ also has a significantly enhanced photothermal effect, which promotes the photocatalytic reaction by increasing the temperature of the reactor. The benefit from the synergistic effect of light and heat, the H_2 evolution rate of $g\text{-C}_3\text{N}_4@Cu_{0.5}In_{0.5}S$ is as high as $2325.68 \mu\text{mol h}^{-1} \text{g}^{-1}$, and the degradation efficiency of oxytetracycline under visible light is 95.7%. The strategy of combining S-scheme heterojunction with photothermal effects provides a promising insight for the development of an efficient photocatalytic reaction.

Keywords: $g\text{-C}_3\text{N}_4@Cu_{0.5}In_{0.5}S$; S-scheme heterojunction; hollow nanostructure; photothermal effect; photocatalysis



Citation: Xiao, Y.; Wang, Z.; Yao, B.; Chen, Y.; Chen, T.; Wang, Y. Hollow $g\text{-C}_3\text{N}_4@Cu_{0.5}In_{0.5}S$ Core-Shell S-Scheme Heterojunction Photothermal Nanoreactors with Broad-Spectrum Response and Enhanced Photocatalytic Performance. *Catalysts* **2023**, *13*, 723. <https://doi.org/10.3390/catal13040723>

Academic Editors: Weilong Shi, Feng Guo, Xue Lin and Yuanzhi Hong

Received: 12 March 2023
Revised: 3 April 2023
Accepted: 6 April 2023
Published: 11 April 2023



Copyright: © 2023 by the authors. Licensee MDPI, Basel, Switzerland. This article is an open access article distributed under the terms and conditions of the Creative Commons Attribution (CC BY) license (<https://creativecommons.org/licenses/by/4.0/>).

1. Introduction

With the development of industry, the problem of energy shortage and environmental pollution is becoming more and more serious [1–3]. It is extremely urgent to develop green, renewable energy and control environmental pollution. The development of photocatalysis technology provides an effective way for the conversion of solar energy into clean fuel and the degradation of organic pollutants [4–7]. The key to the effective use of photocatalysis technology is to develop efficient semiconductor photocatalysts. Graphite phase carbon nitride ($g\text{-C}_3\text{N}_4$) is a new type of conjugated polymeric semiconductor photocatalyst. It has become a new research hotspot in the field of energy conversion and environmental remediation because of its simple synthesis, attractive band structure, high stability, and rich reserves of constituent elements [8–11]. Although $g\text{-C}_3\text{N}_4$ has many excellent properties as a photocatalyst, there are still some shortcomings in the bulk $g\text{-C}_3\text{N}_4$ prepared by direct calcination of precursors: (i) low utilization of the solar spectrum; (ii) serious recombination of the photogenerated carrier; and (iii) a lack of enough active sites on the homogenized surface. Therefore, it is necessary to modify $g\text{-C}_3\text{N}_4$ to improve its photocatalytic activity.

Recombination with narrow band gap semiconductors is one of the effective methods to improve the spectral response of $g\text{-C}_3\text{N}_4$. Different from doping or manufacturing defects, the introduction of narrow band gap semiconductors does not affect the band structure of $g\text{-C}_3\text{N}_4$, which means it has the ability of a broad-spectrum light response while maintaining a strong enough redox ability [12,13]. Huang et al. loaded $g\text{-C}_3\text{N}_4$ nanowires on the surface of ZnIn_2S_4 nanotubes, which effectively expanded the range of the $g\text{-C}_3\text{N}_4$ light response with stronger light absorption capacity and can effectively carry out photocatalytic CO_2 reduction reaction [14]. In addition, some narrow-band gap metal sulfides with strong photothermal effects generate heat by using near-infrared or even infrared sunlight [15,16]. The photothermal effect is rarely considered or even directly ignored in traditional photocatalytic systems, but this part of the energy is very important for the construction of efficient photocatalytic systems. In the heat-assisted photocatalytic reaction based on photochemistry, the catalytic reaction is not directly driven by heat, but this part of the heat can increase the local temperature of the catalyst and help to excite the carrier [17]. Thermal energy can help to further reduce the apparent activation energy of photocatalysis, promote the mobility and mass transfer of photogenerated carriers, and accelerate the transport of materials on the material surface, which is beneficial to increase the rate of the catalytic reaction [18–20].

The morphology of the catalyst affects the exposure of the active site and thus the photocatalytic activity. The low specific surface area of the bulk $g\text{-C}_3\text{N}_4$ leads to the lack of a reactive center. The photocatalyst with a hollow structure has an inner surface and an outer surface, which can provide more active sites [21,22]. Compared with bulk $g\text{-C}_3\text{N}_4$, $g\text{-C}_3\text{N}_4$ with hollow structure has a higher specific surface area and more surface-active centers. In addition, the hollow structure made the distance of charge conduction shorter, reduced the recombination of carriers, enhanced the effects of light scattering and multiple refractions, and improved the absorption and utilization of light [23–26]. More importantly, the well-designed hollow $g\text{-C}_3\text{N}_4$ provides different loading surfaces for both oxidizing and reducing co-catalysts, the electrons, and holes migrate to the outer and inner surfaces, respectively. The wall of the hollow structure acted as a cell membrane, which enabled the spatial separation of redox-active centers on the nanometer scale [27].

The construction of heterojunctions can inhibit the rapid recombination of photogenerated carriers by the charge transfer between semiconductors. In recent years, a new S-scheme heterojunction has been extensively investigated, which drives the spatial separation of carriers by creating an internal electric field [28–30]. S-scheme heterojunctions consist of reduction semiconductors (RS) and oxidation semiconductors (OS), where differences in Fermi energy levels lead to the transfer of electrons from RS to OS, creating internal electric fields and energy band bending at the interface. Under light, the free electrons of photocatalysts are transferred from the conduction band (CB) of OS to the valence band (VB) of RS driven by the internal electric field; at the same time, the band bending prevents the transfer of electrons from RS to OS. This special charge transfer pathway not only suppresses the rapid recombination of electrons and holes but also maintains the strong redox ability of the photocatalyst [31–33]. The $g\text{-C}_3\text{N}_4$ is an ideal reduction semiconductor because of its rather negative CB position. The S-scheme heterojunction formed by oxidation semiconductors with suitable band structures and $g\text{-C}_3\text{N}_4$ not only facilitates charge separation but also enhances the oxidation ability of photocatalysts [34–36]. Fan et al. successfully constructed S-scheme heterostructures with $g\text{-C}_3\text{N}_4$ nanowires and TiO_2 nanoparticles. The low reductive electrons on TiO_2 recombine with holes in $g\text{-C}_3\text{N}_4$ and show effective charge separation and excellent photocatalytic hydrogen production [37].

In this work, we have constructed a hollow $g\text{-C}_3\text{N}_4@Cu_{0.5}In_{0.5}S$ (HCN@CIS) core-shell S-scheme photothermal nanoreactor by combining S-scheme heterojunctions with photothermal effects. Hollow $g\text{-C}_3\text{N}_4$ nanospheres (HCN) were first prepared by the template method and then narrow band gap $Cu_{0.5}In_{0.5}S$ (CIS) nanosheets were grown on its surface. The hollow core-shell structure enhances light absorption, promotes charge separation, and provides more active centers. The photothermal effect converts some of the

light energy into heat, which raises the near-field temperature of the catalyst by radiation and conduction. Benefiting from the effective charge separation and photothermal effect, the HCN@CIS photothermal catalyst offers improved photocatalytic hydrogen production efficiency and excellent oxytetracycline (OTC) degradation performance. In addition, the formation of S-scheme heterojunction is demonstrated by a series of characterization and experiments, and the performance enhancement mechanism of the HCN@CIS photothermal catalyst is analyzed. We believe that this photothermal nanoreactor with fast charge transfer and high efficiency will provide some valuable insights for the development of g-C₃N₄-based photocatalysts for energy conversion and environmental remediation.

2. Results and Discussion

2.1. Morphological and Structural Analysis

The preparation process of the HCN@CIS hollow core-shell nanoreactor is observed by a scanning electron microscope (SEM). Figure S1 shows that the diameter of the SiO₂ nanospheres is about 200 nm, which determines the size of the HCN cavity. Due to the uniform size of the template SiO₂ nanospheres, the prepared HCN morphology is also uniform, and the diameter is about 300 nm (Figure 1a). Figure 1b is a magnified SEM diagram of a single HCN. The notch on the surface shows the typical hollow spherical structure of HCN, and the cross-section of the hollow spherical wall is shown near the notch, which shows the relatively loose particle stacking structure of HCN. The cyanamide is polymerized in SiO₂ mesoporous shell to form g-C₃N₄, and the SiO₂ template forms this stacking shape after being etched. From Figure 1c, the surface of the HCN sphere is wrapped by a CIS nanosheet, which is in the shape of flower ball, and the multi-stage structure of HCN@CIS is more favorable for the exposure of active parts [38,39]. A transmission electron microscope (TEM) can observe this hollow multi-stage core-shell structure more clearly. Figure 1d shows that SiO₂@g-C₃N₄ is a core-shell structure with a dense SiO₂ core and a loose mesoporous SiO₂/g-C₃N₄ shell before the SiO₂ template is etched. The HCN presents a unique hollow spherical structure after the SiO₂ is etched. The cavity size is the same as the dense SiO₂ core, and the thickness of the spherical wall is about 50 nm (Figure 1e). The surface of HCN@CIS still has a hollow structure after the formation of CIS, and the CIS nanosheets are arranged vertically on the surface of the HCN, and the overall size of the nanosphere increases significantly (Figure 1f). Figure 1f,g shows that the thickness of the CIS nanosheets on the surface of the HCN is between 50–100 nm. The lattice fringes of 0.195 nm (Figure 1h,i) can be observed in the high-resolution transmission electron microscope images of HCN@CIS, which can be assigned to the 024 crystal plane of CIS. Figure 1j shows the element distribution map of HCN@CIS, which clearly shows that the distribution of C (red) and N (blue) elements shows the outline of a hollow sphere, and the element groups of Cn (green), In (yellow) and S (purple) are mainly distributed outside the hollow sphere. These results further prove that the HCN@CIS hollow core-shell structure was prepared successfully.

2.2. Phase Structure, Elemental Composition, and Band Structure Analysis

The crystal structure and composition of photocatalysts are studied by X-ray diffraction (XRD). Figure 2a shows that HCN has two diffraction peaks at 13.1° and 27.3°. The two peaks refer to the interlaminar accumulation of aromatic compounds and the in-plane periodic structure of melon compounds, which correspond to the graphite phase carbon nitride (100) and (002) crystal planes, respectively [40,41]. There are three obvious diffraction peaks of CIS at 29.9°, 46.3°, and 55.1°, which correspond to the (112), (024), and (132) crystal planes of Cu_{0.5}In_{0.5}S, respectively. The result is consistent with the characteristic peak in the standard sample Cu_{0.5}In_{0.5}S (JCPDS No.47-1372). The diffraction peak of HCN@CIS contained all the characteristic peaks of HCN and CIS, indicating that CIS is successfully loaded on HCN. Figure 2b is the survey X-ray photoelectron spectroscopy (XPS) of HCN, CIS, and HCN@CIS. The C and N elements are visible in the survey XPS spectrum of HCN, the survey XPS spectrum of HCN contains the signals of S,

In, and Cu elements, and the survey XPS spectrum of HCN@CIS contains the characteristic signals of HCN and CIS, which further indicates that the HCN@CIS composite has been prepared successfully. UV-visible diffuse reflectance spectroscopy (UV-vis DRS) is used to analyze the spectral absorption properties and determine the absorption edge of the powder photocatalysts. Figure 2c shows that the light absorption threshold of HCN is about 470 nm, which can absorb ultraviolet light and part of visible light. The CIS has a broad-spectrum response capability that covers almost the whole spectrum, which is related to its narrow band gap and dark characteristics [42]. Compared with the original HCN, the absorption range of HCN@CIS is significantly expanded and still has a strong spectral response in the visible-near infrared region. Figure 2d shows the optical band gap (E_g) of HCN and CIS are 2.61 eV and 2.17 eV, respectively. The valence band energies of HCN and CIS measured by XPS valence band spectroscopy (VB-XPS) are 1.31 eV and 1.52 eV, respectively. The energy of the samples relative to the standard hydrogen electrode (E_{NHE}) is calculated by the following formula: $E_{NHE} = \varphi + E_{VB-XPS} - 4.44$, where φ is the work function of the instrument (4.5 eV); therefore, the valence band energy of HCN and CIS relative to the standard hydrogen electrode is about 1.37 and 1.58 eV [43]. According to the relationship between the E_{CB} potential and E_g ($E_{CB} = E_{VB} - E_g$), the CB potentials of HCN and CIS are determined to be -1.19 eV and -0.24 eV, respectively. Therefore, the band structure arrangement of HCN and CIS can be determined as shown in Figure 2f. The CB position of CIS is between CB and VB of HCN, and the VB position of HCN is between CB and VB of CIS, which accords with the staggered energy level arrangement and meets the formation basis of S-scheme heterojunction [44].

2.3. Charge Transfer Pathways of Catalysts

The work function of a semiconductor represents the minimum energy required for an electron in a semiconductor whose energy is equal to the Fermi level to escape into a vacuum. A large work function means that it is difficult for the electrons to leave the semiconductor and a smaller one means that the semiconductor is prone to losing electrons. Therefore, the possible electron transfer pathways of the contact interface of the two kinds of semiconductors can be studied by measuring the work function [45]. The relative surface potential of HCN and CIS are measured by a scanning kelvin probe (SKP), and the real work function is calculated by the difference between the semiconductor surface and the highly sensitive probe [46]. Figure 3a shows that the surface potential of Au, HCN, and CIS are 127.87 eV, -103.02 eV, and -562.13 eV, respectively. The real work function of the Au is 5.1 eV; therefore, the real work functions of HCN and CIS are 4.41 eV and 4.83 eV, respectively. The Fermi level of CIS is relatively lower than that of HCN, and the electrons on HCN will transfer to CIS when they are contacted. As a highly sensitive analytical method, XPS can identify the changes in element binding energy and chemical environment in materials. The change in binding energy is closely related to the changes in electron density and element valence state. Normally, if a material loses electrons, its binding energy moves to a higher energy, and when it gains electrons, the binding energy moves to a lower energy [47]. Figure 3b shows the high-resolution XPS spectrum of C1s. The peak at 284.8 eV is an indeterminate carbon. The peaks at 286.5 and 288.34 eV in HCN correspond to C-N and N-C=N, respectively. The peaks of binding energies 398.24 eV, 400.08 eV, and 401.02 eV in the N1s spectra are attributed to sp^2 coordination nitrogen (N-C=N), tertiary nitrogen (N-(C)₃), and surface amino group (N-H_x) (Figure 3c) [48]. The peaks of Cu 2p in CIS at 931.79 eV and 951.68 eV correspond to Cu 2p_{3/2} and Cu 2p_{1/2}, respectively (Figure 3d) [49]. The two peaks at 444.72 eV and 452.35 eV are attributed to the In 3d_{3/2} and 3d_{1/2}, respectively (Figure 3e). The S 2p spectrum in Figure 3f is fitted into two peaks, S 2p_{3/2} (161.76 eV) and S 2p_{1/2} (163.05 eV). Figure 3b–f shows that the binding energy of C and N elements in the HCN@CIS samples increases when the heterojunction is formed, which indicates the loss of electrons in HCN. The binding energies of C and N elements in HCN@CIS samples shift to low energy under light, indicating that HCN obtains electrons again. Correspondingly, the binding energies of Cu, In, and S in HCN@CIS increase after

contact, indicating that the electrons lost by HCN are transferred to CIS. The binding energy of Cu, In, and S elements in HCN@CIS samples shifts to a high energy under light, indicating that the electrons on the CIS flow back to the HCN. The results of in situ irradiation of XPS further verified the charge transfer mechanism in HCN@CIS [50]. When the HCN and CIS come into contact, the free electrons on the HCN will be transferred to the CIS through the contact interface until the Fermi level is balanced. At this time, electrons accumulate on the CIS and a large number of holes remain on the HCN. Therefore, an internal electric field orienting from the HCN to the CIS is formed. Due to charge interactions, the band of the HCN at the interface bends upward, while the band of the ZIS bends downward. The HCN and CIS are excited by light to produce carriers. Under the action of the internal electric field and band bending, the electrons in the CB of the CIS will recombine with the holes in the VB of the HCN, thus completing the charge transfer of the S-scheme pathway.

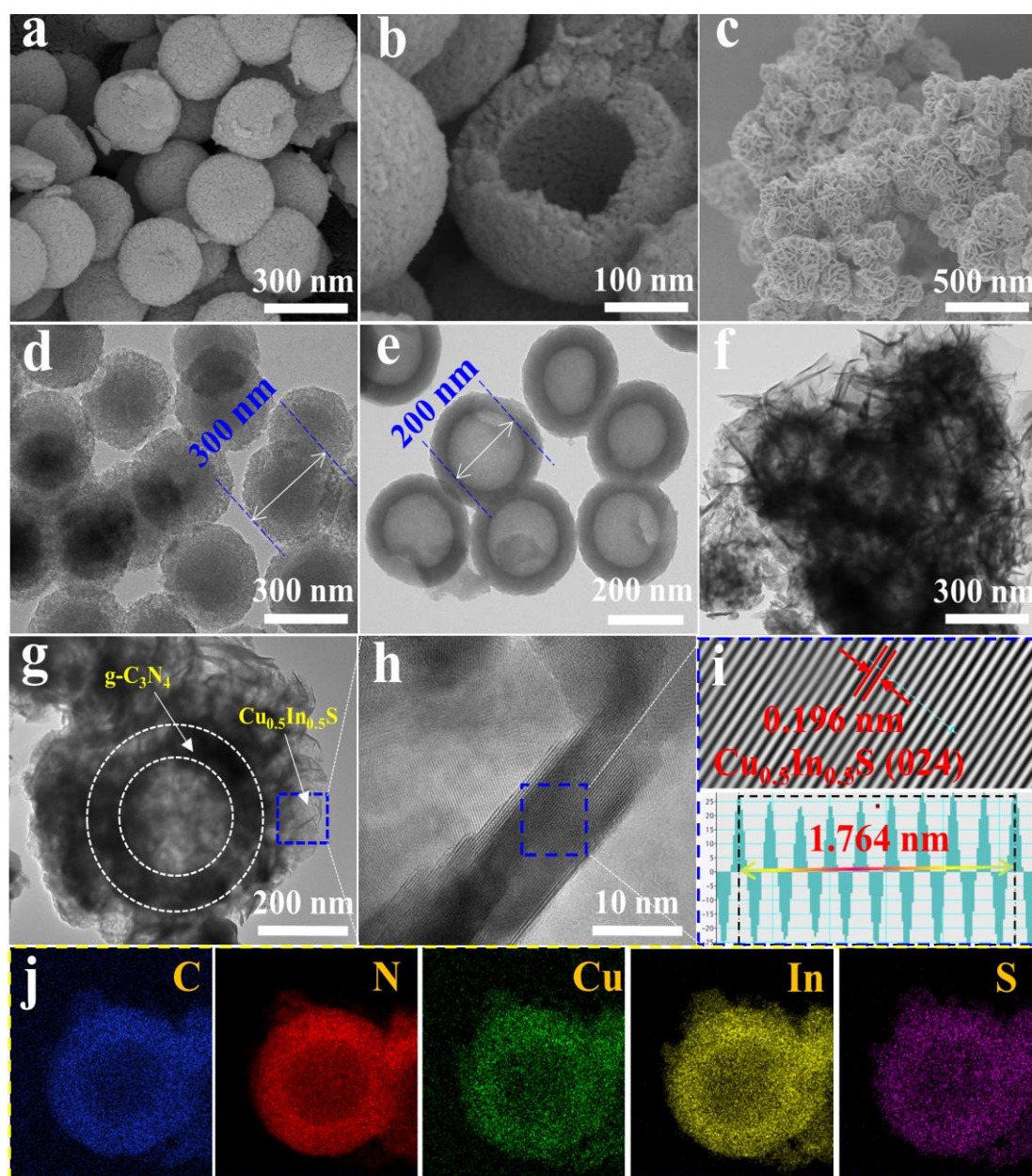


Figure 1. SEM images of HCN (a,b) and HCN@CIS (c). TEM images of SiO₂@g-C₃N₄ (d), HCN (e), and HCN@CIS (f,g). HRTEM images of HCN@ZIS (h,i). Elemental mapping images of HCN@CIS (j).

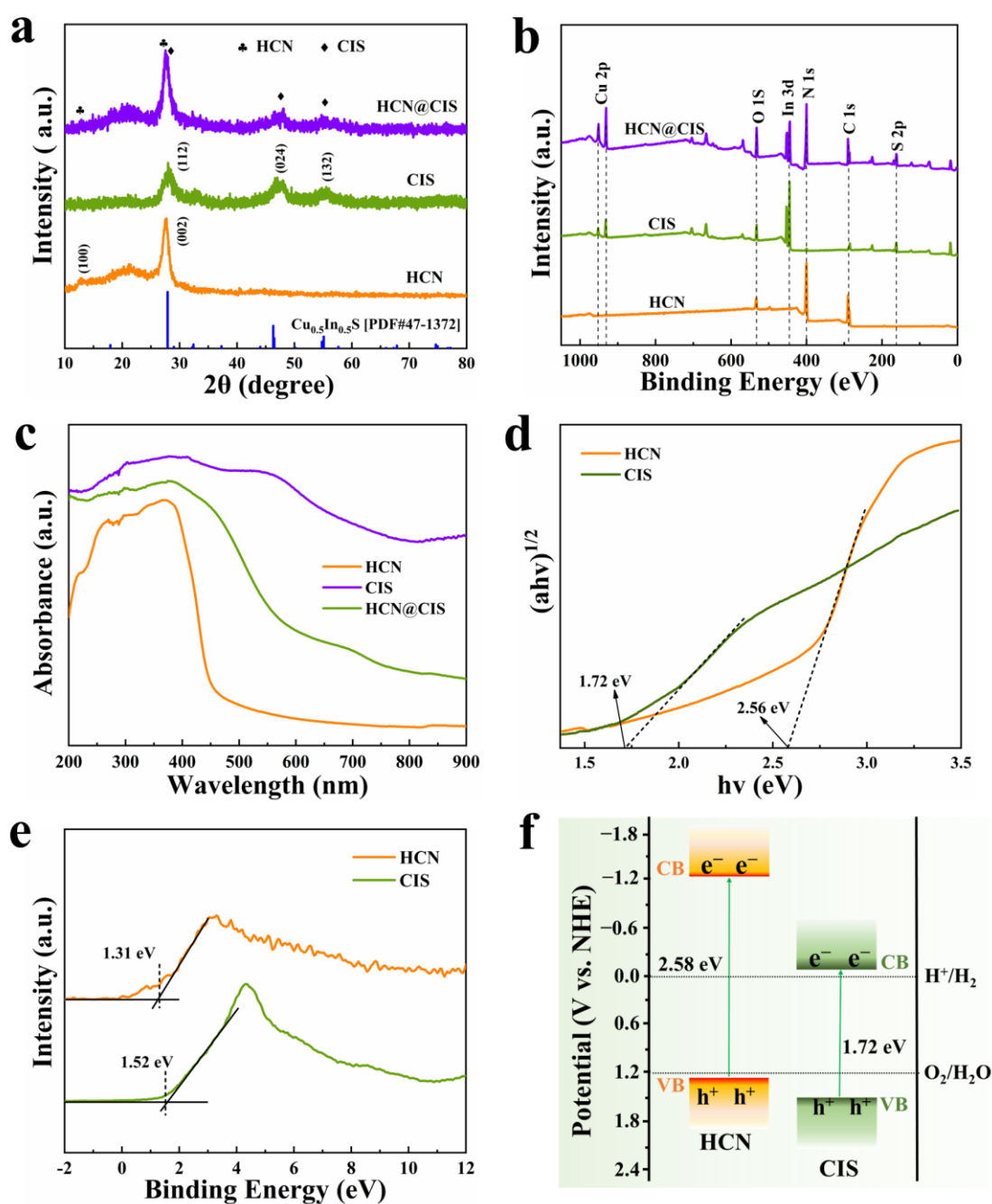


Figure 2. XRD pattern (a), XPS spectra (b), and UV-vis spectra (c) of HCN, CIS, and HCN@CIS. Tauc plots (d) and VB-XPS spectra (e) of HCN and CIS. Band structure alignments of HCN and CIS (f).

2.4. Photothermal Properties of Catalysts

The Arrhenius formula shows that the chemical reaction rate is positively related to the reaction temperature, so the photothermal effect of a photocatalyst can promote the catalytic reaction [51]. The change in temperature of the powder photocatalyst with illumination time was recorded by an infrared camera. A 300 W xenon lamp illuminates the powder photocatalyst vertically at a distance of 30 cm. The initial temperature of the HCN powder is 21.7 °C. After 90 s of irradiation, the surface temperature rises to 62.7 °C (Figure 4a), and the surface temperature increased by 41 °C. Under the same conditions, the heating range of the CIS powder is 116.2 °C, which is 2.8 times that of the HCN. The strong photothermal effect of CIS is related to its narrow band gap and dark color, which is easy to absorb light (Figure S3). It is worth noting that after 90 s of irradiation, the surface

temperature of HCN@CIS powder increases from 22.8 °C to 153 °C, which is 3.2 times higher than that of pure HCN and 14 °C higher than that of pure CIS. This may be due to the layered structure formed by the CIS arranged vertically on the HCN surface, facilitating enhanced light absorption. The multiple reflections and absorptions in the hollow structure are also reasons for the improvement of the photothermal performance of HCN@CIS. In addition, the rapid carrier transfer process between heterojunctions can also convert part of the mechanical energy into thermal energy [52]. The unique hollow core-shell structure of HCN@CIS provides a basis for the effective utilization of heat generated by the photothermal effect. We assume that the heat generated by the photothermal effect of HCN@CIS spreads to the external aqueous solution and the internal space at the same time. It is difficult to increase the overall temperature of the solution by the photothermal effect alone, but there is only a small amount of water inside the hollow sphere that needs to be heated. Therefore, under the action of double shell heat preservation and heat collection, the internal temperature of the HCN@CIS reactor should be much higher than that of the external solution [53]. The increase in HCN@CIS temperature will accelerate the movement of surrounding water molecules, which is beneficial to increase the collision probability of carriers and active radicals with reactant molecules and improve the photocatalytic reaction rate by promoting local mass transfer kinetics.

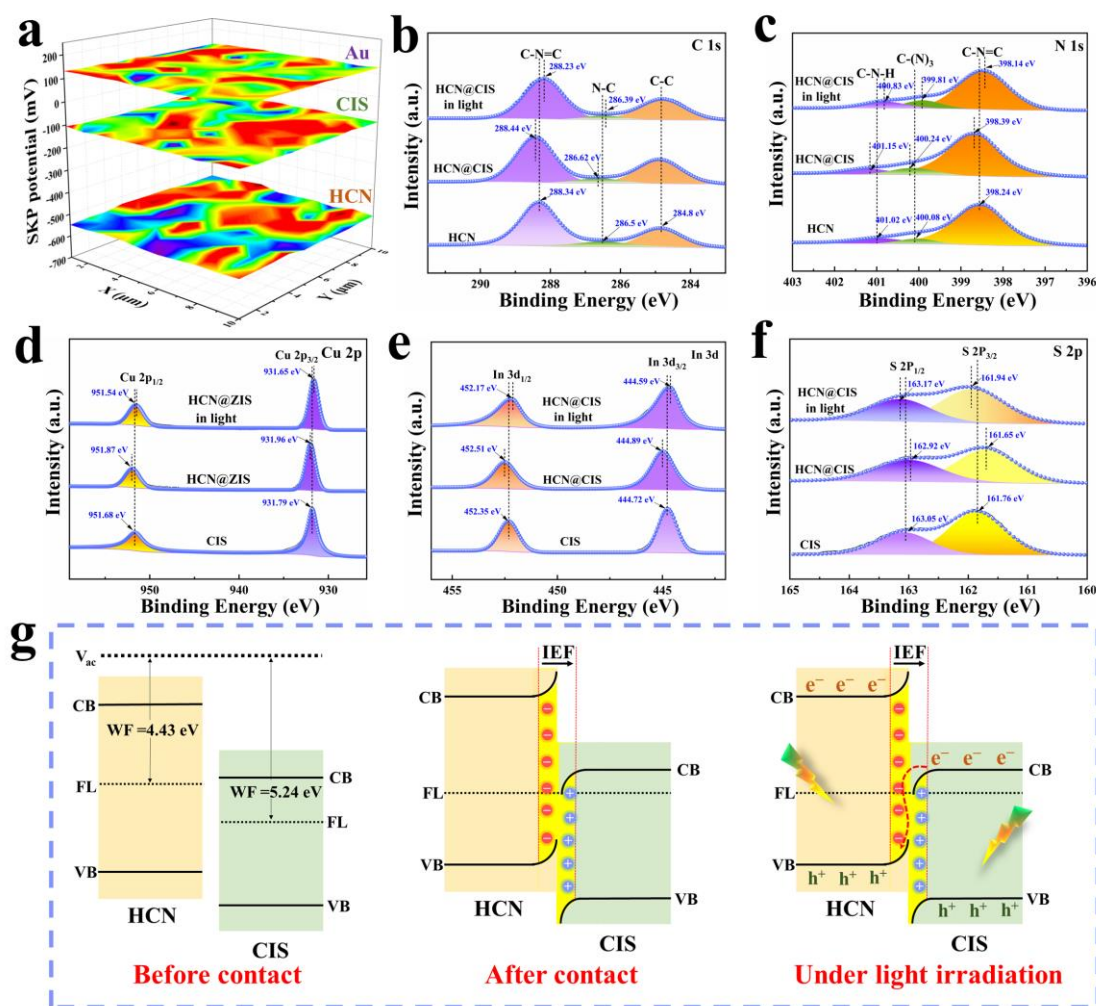


Figure 3. (a) Work functions of the HCN and the CIS. XPS spectra of C 1s (b) and N 1s (c) of the HCN and the HCN@CIS. XPS spectra of Cu 1s (d), In 2p (e), and S 1s (f) of the CIS and the HCN@CIS. Schematic representation of the formation process and charge transfer mechanism of the HCN@CIS S-scheme heterojunction (g).

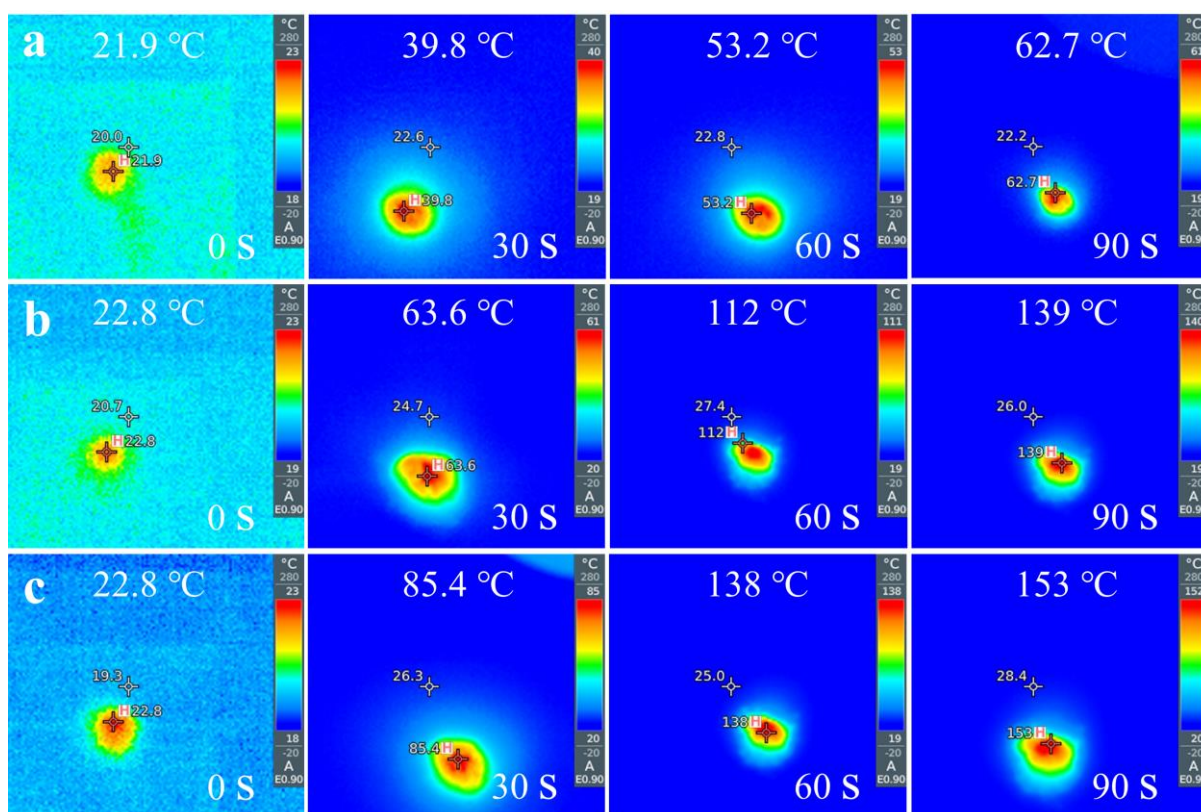


Figure 4. The IR images of temperature variation with light time for HCN (a), CIS (b), and HCN@CIS (c) (The light source is a 300 W Xe lamp with a 420 nm filter).

2.5. Photocatalytic H₂ Production and Pollutant Removal

Figure 5a shows the photocatalytic H₂ production performance of the different samples. HCN@CIS with 20% CIS load has the best photocatalytic H₂ production performance (unless otherwise specified, the HCN@ZIS in this paper refers to the optimum sample), and the hydrogen production rate is as high as 2325.68 $\mu\text{mol h}^{-1} \text{g}^{-1}$, which is 62.8 and 12.2 times higher than that of pure HCN and CIS, respectively. Compared with other heterojunction photocatalysts reported recently, the HCN@CIS has excellent performance for H₂ evolution (Table S1). The HCN@CIS shows excellent stability in the 20 h cycle test (Figure 5b). There are two reasons why the HCN@ZIS sample has good hydrogen production performance. On the one hand, the S-scheme heterojunction provides fast carrier separation efficiency, and on the other hand, the photothermal effect activates the water molecules in the cavity, which promotes the evolution of active H* species and accelerates the formation of H₂ [9]. Figure 5c shows the photocatalytic degradation curves of different samples for OTC. The solution reached dynamic adsorption equilibrium after the reaction was conducted in the dark for 30 min, and then the

Photocatalytic degradation experiment was carried out. It can be seen that the HCN@CIS with a 20% ZIS load has the best degradation effect of OTC, and the degradation rate in 120 min is as high as 95.7%, indicating that the reaction active site can be fully exposed with an appropriate load. Figure 5d shows that the apparent reaction rate of the HCN@CIS is 9.4 and 5.9 times higher that of pure HCN and ZIS, respectively, indicating that the efficient charge separation of the S-scheme heterojunction can improve the photocatalytic reaction rate. In addition, the HCN@CIS composite photocatalyst has excellent stability, with only a slight decrease in degradation efficiency after 600 min of cycling (Figure 5e). The active species in photocatalytic reactions are analyzed by a radical quenching experiment. Benzoquinone (BQ), silver nitrate (AgNO₃), triethanolamine (TEOA), and isopropanol (IPA) were used as quenching agents of $\cdot\text{O}_2^-$, e^- , h^+ and $\cdot\text{OH}$, respectively [54]. It can be seen from Figure 5f that the contribution rate of free radicals

in the process of photocatalysis is $\cdot\text{O}_2^- > e^- > h^+ > \cdot\text{OH}$. Among them, $\cdot\text{O}_2^-$, e^- , and h^+ play an important role, and electron trapping may decrease the yield of $\cdot\text{O}_2^-$ and affect the photocatalytic activity. The VB potential of CIS in HCN@CIS is not enough to oxidize water to produce $\cdot\text{OH}$, so the addition of IPA has almost no effect on the efficiency of photocatalytic degradation.

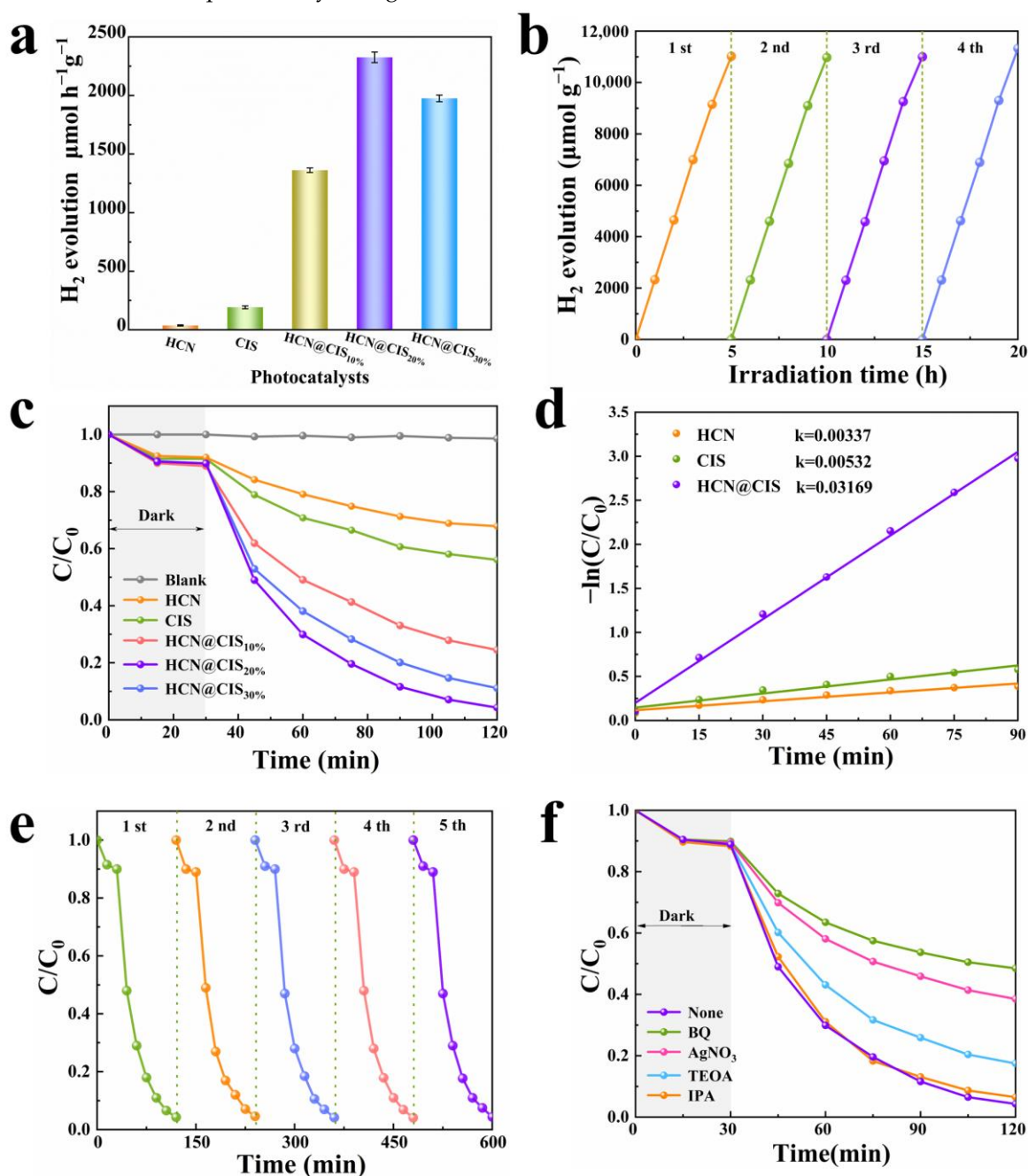


Figure 5. Photocatalytic H₂ evolution for all samples (a) and H₂ production cycle test of HCN@CIS (b). Photocatalytic degradation of OTC for all samples (c) and the corresponding apparent reaction rate constants k (d). Cycling tests (e) and free radical quenching experiments (f) on HCN@CIS degraded OTC.

2.6. Analysis of Charge-Transfer Dynamics

The photoelectrochemical test is used to analyze the charge separation characteristics in the photocatalyst. Figure 6a shows the photocurrent response curve obtained by a cyclic switching light source, and the HCN@CIS shows the highest current density, indicating that

the S-scheme heterojunction has better charge separation ability [55,56]. Electrochemical impedance spectroscopy (EIS) shows that the radius of the Nyquist curve of HCN@CIS is the smallest (Figure 6b), which means that the resistance of surface charge transfer is lower, which is beneficial to rapid carrier separation and transfer [57]. The kinetics of charge transfer of the photocatalysts is closely related to the catalytic performance. Figure S4 shows the steady-state photoluminescence (PL) emission spectra of HCN, CIS, and HCN@CIS. It can be seen that the fluorescence quenching intensity of HCN@CIS is much lower than that of pure HCN and CIS, which indicates that S-scheme heterojunctions effectively reduce the recombination of photogenerated carriers [58,59]. The charge transfer kinetics at the interface are further analyzed by time-resolved photoluminescence (TRPL) spectra. The TRPL kinetic spectra of HCN, CIS, and HCN@CIS are shown in Figure 6c. The normalized results show that the average PL lifetime of HCN@CIS (3.57 ns) is longer than that of pure HCN (1.97 ns) and CIS (2.23 ns). The longer carrier lifetime in S-scheme heterojunctions is beneficial to the full contact of electrons and holes with surface adsorption molecules and improves the effective utilization of photogenerated carriers [60]. The analysis of the active species and content of photocatalytic production is considered an important means to determine the mechanism of photocatalysis. The VB of HCN@CIS is not enough to oxidize H_2O to form $\cdot\text{OH}$, so the $\cdot\text{O}_2^-$ spin signal produced in the process of the photocatalysis is detected by the electron spin resonance (EPR) technique and DMPO (5-dimethyl-1-proline-N-oxide) as spin trap. Figure 6d shows that HCN, CIS, and HCN@CIS can all produce $\cdot\text{O}_2^-$, but the HCN@CIS $\cdot\text{O}_2^-$ spin signal is the strongest. The reduction of O_2 adsorbed on the surface by conduction band electrons of the photocatalyst affects the formation of $\cdot\text{O}_2^-$. The HCN@CIS can produce $\cdot\text{O}_2^-$ more efficiently, indicating that the electron reduction ability of the CB of the HCN@CIS composite photocatalyst has not decreased, and the possibility of forming Type-II heterojunction between HCN and CIS can be ruled out [61]. The interlaced HCN and CIS follow the S-scheme charge-transfer mechanism. The rapid charge separation and excellent photothermal properties of HCN@CIS promote the mass transfer kinetics of the reaction system and accelerate the formation of $\cdot\text{O}_2^-$.

Based on a large number of characterization and photocatalytic experiments, the photocatalytic performance enhancement mechanism of the HCN@CIS heterojunction photothermal nanoreactor (Scheme 1) was proposed. The HCN@CIS with a unique hollow core-shell structure generates carriers excited by light, and the carriers follow S-scheme migration under the action of an internal electric field and interface band bending. The electrons in the CB of the CIS recombine with the holes in the VB of the HCN. The electrons with strong reduction ability in the CB of the HCN and the holes with strong oxidation ability in the VB of the CIS are successfully retained in the HCN@CIS system. In addition, the hollow structure can improve the utilization of light, and the double shell can inhibit the rapid escape of internal heat, provide a local high-temperature place, and accelerate the reaction kinetics. The free electrons in HCN@CIS are retained on the inner HCN, and the energy of the photothermal effect is gathered in the inner space. Therefore, the HCN@CIS photothermal nanoreactor can efficiently carry out photocatalytic hydrogen production and photocatalytic degradation of oxytetracycline by the synergistic action of S-scheme heterojunction and the photothermal effect.

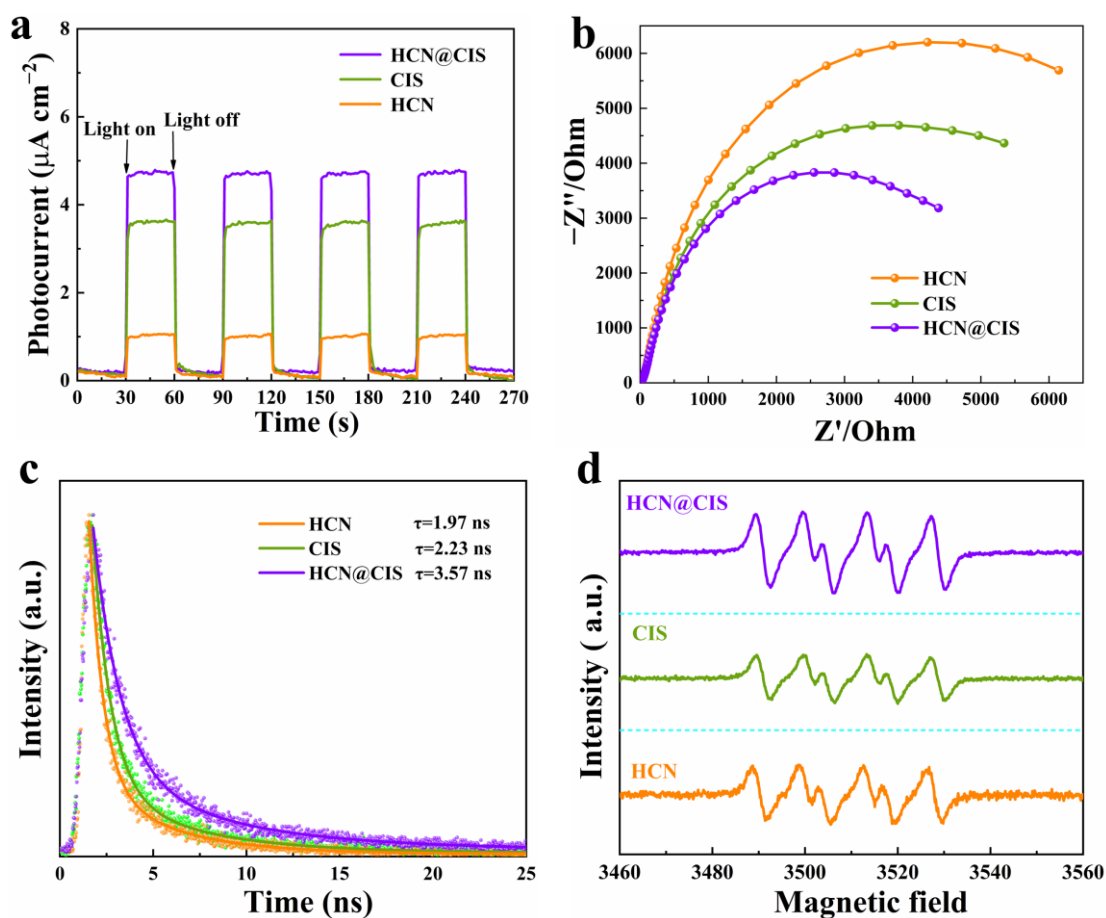
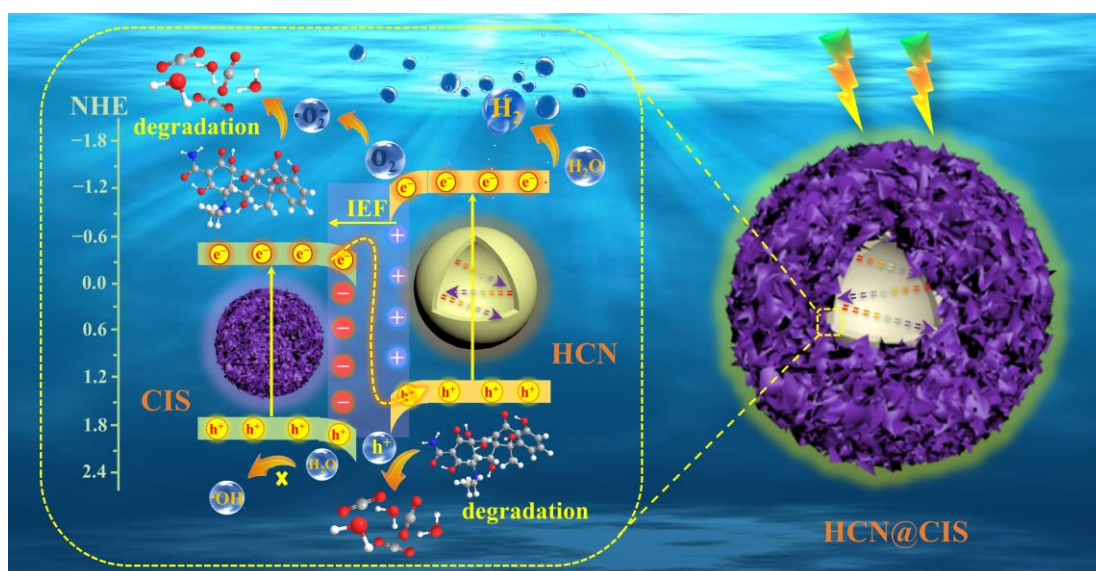


Figure 6. Transient photocurrent density curves (a), EIS Nyquist plots (b), and TRPL decay spectra (c) of HCN, CIS, and HCN@CIS. EPR signals of HCN, CIS, and HCN@CIS in light (d).

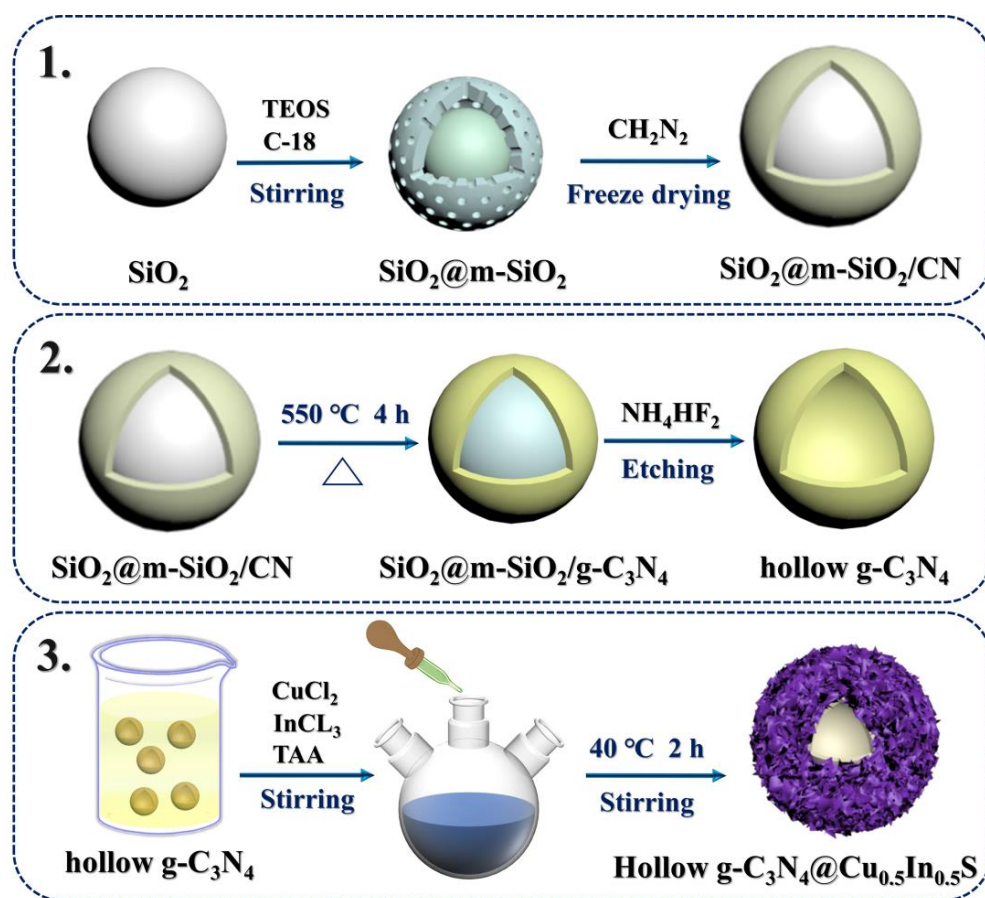


Scheme 1. Schematic diagram of the HCN@CIS S-scheme hollow core-shell nanoreactor for photocatalytic H_2 production and OTC degradation.

3. Materials and Methods

The chemical reagents and auxiliary materials used in this study are listed in Supporting Information. The chemical reagents are not further treated before use. The steps for the syn-

thesis of the SiO₂ template, HCN, and HCN@CIS are shown in Scheme 2. The characterization parameters and experimental details are in Supporting Information, respectively.



Scheme 2. The schematic diagram for the preparation of the HCN@CIS hollow core-shell nanoreactor. (1) Preparation of mesoporous SiO₂/SiO₂@CN nanospheres, (2) Synthesis of HCN nanospheres, (3) Preparation of the HCN@CIS core-shell nanoreactor.

3.1. Preparation of Mesoporous SiO₂/SiO₂ Nanospheres

SiO₂ nanosphere templates are prepared by the Stöber method. Typical synthesis methods are as follows: 3.5 mL of TEOS was dropped into the mixed solution of 7.0 mL NH₃·H₂O, 16.5 mL H₂O, and 110 mL C₂H₅OH under magnetic stirring and stirred at room temperature for 2 h to form uniformly dispersed silica spheres. C18-TMOS and TEOS were mixed at a ratio of 2:3 by volume, then dripped into the mixed solution and aged at room temperature for 3 h. The mixed solution was centrifuged, dried at 60 °C, and calcined at 550 °C for 6 h to obtain mesoporous SiO₂/SiO₂ nanospheres.

3.2. Synthesis of HCN Nanospheres

The 2 g mesoporous SiO₂/SiO₂ template was added to the 10 mL cyanamide solution, ultrasonic for 2 h, stirred at 60 °C for 6 h, then centrifuged, washed, and freeze-dried. The dried white powder was placed in a tube furnace, calcined at 550 °C for 4 h under the protection of nitrogen, and the heating rate was 5 °C/min. The gray-white powder was SiO₂@g-C₃N₄, and the SiO₂ template was etched with 4 mol/L NH₄HF₂ solution. Light yellow HCN can be obtained by centrifugation and drying.

3.3. Preparation of the HCN@CIS Core-Shell Nanoreactor

In typical synthesis, the prepared HCN (0.1 g) was added to three beakers containing 40 mL deionized water, respectively, and dispersed by ultrasonic for 30 min, then 0.007 g

CuCl₂·2H₂O, 0.012 g InCl₃·4H₂O, and 0.006 g TAA (10 wt%); 0.017 g CuCl₂·2H₂O, 0.024 g InCl₃·4H₂O, and 0.012 g TAA (20 wt%); 0.021 g CuCl₂·2H₂O, 0.036 g InCl₃·4H₂O, and 0.018 g TAA (30 wt%) were added to 3 beakers under magnetic stirring, respectively (x wt% represents the percentage of Cu_{0.5}In_{0.5}S mass to g-C₃N₄), and the solution pH was adjusted to 2.5 with hydrochloric acid. The mixed solution was transferred to a 150 mL round-bottom flask and refluxed in an oil bath at 40 °C for 2 h. Centrifuge and dry the powder at 60 °C overnight to obtain a black HCN@CIS hollow core-shell nanoreactor.

4. Conclusions

In summary, HCN hollow nanospheres are obtained by the template method, and the hollow HCN@CIS core-shell S-scheme photothermal nanoreactors are obtained by surface continuous growth. The charge-transfer mechanism of the S-scheme in HCN@ZIS was proved by in situ irradiation, XPS, and EPR characterization. In addition, the synergistic effect of the photothermal effect and S-scheme heterojunction on photocatalytic reactions is proposed. The fast charge transfer and redox ability of S-scheme heterojunctions intensely initiate the photocatalytic reaction, and the photothermal effect reduces the activation energy barrier of the chemical reaction and speeds up the reaction rate. Therefore, HCN@CIS has enhanced photothermal catalytic activity, and the photocatalytic H₂ evolution efficiency is 62.8 and 12.2 times higher than that of pure HCN and CIS, respectively, and the degradation efficiency of oxytetracycline is as high as 95.7%. This work fully demonstrates the potential of the synergistic effect of S-scheme heterojunction and photothermal effect and provides a promising strategy for the design of an efficient solar-driven photothermal catalyst platform.

Supplementary Materials: The following supporting information can be downloaded at: <https://www.mdpi.com/article/10.3390/catal13040723/s1>, Figure S1: SEM image of the SiO₂ spheres; Figure S2: TEM image of SiO₂@g-C₃N₄; Figure S3: The sample patterns of HCN, CIS and HCN@CIS; Figure S4: PL emission spectra of HCN, CIS and HCN@CIS; Table S1: Comparison of H₂ generation rates of different photocatalysts. References [62–68] were cited in the Supplementary Materials.

Author Contributions: Y.X.: Data curation, Investigation, Writing—original draft, Methodology. Z.W.: Methodology, Visualization, Writing—review & editing. B.Y.: Writing—review & editing. Y.C.: Supervision. T.C.: Writing—review & editing. Y.W.: Funding acquisition, Writing—review & editing. All authors have read and agreed to the published version of the manuscript.

Funding: This research was funded by Yunnan University's Research Innovation Fund for Graduate Students (KC.22222464).

Data Availability Statement: The data that support the findings of this study are available from the corresponding author upon reasonable request.

Acknowledgments: We gratefully acknowledge the support of this research by the National Natural Science Foundation of China (Nos. 41876055 and 61761047), Yunnan University's Research Innovation Fund for Graduate Students (KC.22222464), and the Program for Innovative Research Team (in Science and Technology) at the University of Yunnan Province.

Conflicts of Interest: The authors declare no conflict of interest.

References

1. Nishiyama, H.; Yamada, T.; Nakabayashi, M.; Maehara, Y.; Yamaguchi, M.; Kuromiya, Y.; Nagatsuma, Y.; Tokudome, H.; Akiyama, S.; Watanabe, T.; et al. Photocatalytic solar hydrogen production from water on a 100-m² scale. *Nature* **2021**, *598*, 304–307. [[CrossRef](#)] [[PubMed](#)]
2. Zhou, P.; Navid, I.A.; Ma, Y.; Xiao, Y.; Wang, P.; Ye, Z.; Zhou, B.; Sun, K.; Mi, Z. Solar-to-hydrogen efficiency of more than 9% in photocatalytic water splitting. *Nature* **2023**, *613*, 66–70. [[CrossRef](#)] [[PubMed](#)]
3. Nikoloudakis, E.; López-Duarte, I.; Charalambidis, G.; Ladomenou, K.; Ince, M.; Coutsolelos, A.G. Porphyrins and phthalocyanines as biomimetic tools for photocatalytic H₂ production and CO₂ reduction. *Chem. Soc. Rev.* **2022**, *51*, 6965–7045. [[CrossRef](#)] [[PubMed](#)]
4. Fang, Y.; Hou, Y.; Fu, X.; Wang, X. Semiconducting polymers for oxygen evolution reaction under light illumination. *Chem. Rev.* **2022**, *122*, 4204–4256. [[CrossRef](#)] [[PubMed](#)]

5. Kosco, J.; Gonzalez-Carrero, S.; Howells, C.T.; Fei, T.; Dong, Y.; Sougrat, R.; Harrison, G.T.; Firdaus, Y.; Sheelamanthula, R.; Purushothaman, B.; et al. Generation of long-lived charges in organic semiconductor heterojunction nanoparticles for efficient photocatalytic hydrogen evolution. *Nat. Energy* **2022**, *7*, 340–351. [[CrossRef](#)]
6. Pavliuk, M.V.; Wrede, S.; Liu, A.; Brnovic, A.; Sicong Wang, S.; Axelssona, M.; Tian, H. Preparation, characterization, evaluation and mechanistic study of organic polymer nano-photocatalysts for solar fuel production. *Chem. Soc. Rev.* **2022**, *51*, 6909–6935. [[CrossRef](#)]
7. Tao, X.; Zhao, Y.; Wang, S.; Li, C.; Li, R. Recent advances and perspectives for solar-driven water splitting using particulate photocatalysts. *Chem. Soc. Rev.* **2022**, *51*, 3561–3608. [[CrossRef](#)]
8. Teng, Z.; Zhang, Q.; Yang, H.; Kato, K.; Yang, W.; Lu, Y.-R.; Liu, S.; Wang, C.; Yamakata, A.; Su, C.; et al. Atomically dispersed antimony on carbon nitride for the artificial photosynthesis of hydrogen peroxide. *Nat. Catal.* **2021**, *4*, 374–384. [[CrossRef](#)]
9. Liu, P.; Huang, Z.; Gao, X.; Hong, X.; Zhu, J.; Wang, G.; Wu, Y.; Zeng, J.; Zheng, X. Synergy between palladium single atoms and nanoparticles via hydrogen spillover for enhancing CO₂ photoreduction to CH₄. *Adv. Mater.* **2022**, *34*, 2200057. [[CrossRef](#)]
10. Xie, W.; Li, K.; Liu, X.H.; Zhang, X.; Huang, H. P-Mediated Cu–N₄ Sites in Carbon Nitride Realizing CO₂ Photoreduction to C₂H₄ with Selectivity Modulation. *Adv. Mater.* **2023**, *35*, 2208132. [[CrossRef](#)]
11. Qian, W.; Hu, W.; Jiang, Z.; Wu, Y.; Li, Z.; Diao, Z.; Li, M. Degradation of Tetracycline Hydrochloride by a Novel CDs/g-C₃N₄/BiPO₄ under Visible-Light Irradiation: Reactivity and Mechanism. *Catalysts* **2022**, *12*, 774. [[CrossRef](#)]
12. Xie, P.; Ding, J.; Yao, Z.; Pu, T.; Zhang, P.; Huang, Z.; Wang, C.; Zhang, J.; Zecher-Freeman, N.; Zong, H.; et al. Oxo dicopper anchored on carbon nitride for selective oxidation of methane. *Nat. Commun.* **2022**, *13*, 1375. [[CrossRef](#)] [[PubMed](#)]
13. Gao, R.H.; Ge, Q.; Jiang, N.; Cong, H.; Liu, M.; Zhang, Y.Q. Graphitic carbon nitride (g-C₃N₄)-based photocatalytic materials for hydrogen evolution. *Front. Chem.* **2022**, *10*, 1048504. [[CrossRef](#)] [[PubMed](#)]
14. Li, L.; Ma, D.; Xu, Q.; Huang, S. Constructing hierarchical ZnIn₂S₄/g-C₃N₄ S-scheme heterojunction for boosted CO₂ photoreduction performance. *Chem. Eng. J.* **2022**, *437*, 135153. [[CrossRef](#)]
15. Yang, T.; Shao, Y.; Hu, J.; Qu, J.; Yang, X.; Yang, F.; Li, C.M. Ultrathin layered 2D/2D heterojunction of ReS₂/high-crystalline g-C₃N₄ for significantly improved photocatalytic hydrogen evolution. *Chem. Eng. J.* **2022**, *448*, 137613. [[CrossRef](#)]
16. Chen, Y.; Su, F.; Xie, H.; Wang, R.; Ding, C.; Huang, J.; Xu, Y.; Ye, L. One-step construction of S-scheme heterojunctions of N-doped MoS₂ and S-doped g-C₃N₄ for enhanced photocatalytic hydrogen evolution. *Chem. Eng. J.* **2021**, *404*, 126498. [[CrossRef](#)]
17. Wang, Z.; Yang, Z.; Fang, R.; Yan, Y.; Ran, J.; Zhang, L. A State-of-the-art review on action mechanism of photothermal catalytic reduction of CO₂ in full solar spectrum. *Chem. Eng. J.* **2022**, *429*, 132322. [[CrossRef](#)]
18. Song, C.; Wang, Z.; Yin, Z.; Xiao, D.; Ma, D. Principles and applications of photothermal catalysis. *Chem. Catal.* **2021**, *2*, 52–83. [[CrossRef](#)]
19. Zhu, J.; Shao, W.; Li, X.; Jiao, X.; Zhu, J.; Sun, Y.; Xie, Y. Asymmetric triple-atom sites confined in ternary oxide enabling selective CO₂ photothermal reduction to acetate. *J. Am. Chem. Soc.* **2021**, *143*, 18233–18241. [[CrossRef](#)]
20. Xiao, Y.; Yao, B.; Wang, Z.; Chen, T.; Xiao, X.; Wang, Y. Plasma Ag-Modified α -Fe₂O₃/g-C₃N₄ Self-Assembled S-Scheme Heterojunctions with Enhanced Photothermal-Photocatalytic-Fenton Performances. *Nanomaterials* **2022**, *12*, 4212. [[CrossRef](#)]
21. Zhang, L.; Wang, Z.Q.; Liao, J.; Zhang, X.; Feng, D.; Deng, H.; Ge, C. Infrared-to-visible energy transfer photocatalysis over black phosphorus quantum dots/carbon nitride. *Chem. Eng. J.* **2022**, *431*, 133453. [[CrossRef](#)]
22. Zheng, D.; Pang, C.; Liu, Y.; Wang, X. Shell-engineering of hollow gC₃N₄ nanospheres via copolymerization for photocatalytic hydrogen evolution. *Chem. Commun.* **2015**, *51*, 9706–9709. [[CrossRef](#)] [[PubMed](#)]
23. Wang, Y.; Liu, M.; Wu, C.; Gao, P.; Li, M.; Xing, Z.; Li, Z.; Zhou, W. Hollow Nanoboxes Cu_{2-x}S@ZnIn₂S₄ Core-Shell S-Scheme Heterojunction with Broad-Spectrum Response and Enhanced Photothermal-Photocatalytic Performance. *Small* **2022**, *18*, 2202544. [[CrossRef](#)] [[PubMed](#)]
24. Tahir, B.; Tahir, M.; Nawawai, M.G.M.; Khoja, A.H.; Haq, B.U.; Farooq, W. Ru-embedded 3D g-C₃N₄ hollow nanosheets (3D CNHNS) with proficient charge transfer for stimulating photocatalytic H₂ production. *Int. J. Hydrog. Energy* **2021**, *46*, 27997–28010. [[CrossRef](#)]
25. Zhang, Y.; Wu, Y.; Wan, L.; Ding, H.; Li, H.; Wang, X.; Zhang, W. Hollow core-shell Co₉S₈@ZnIn₂S₄/CdS nanoreactor for efficient photothermal effect and CO₂ photoreduction. *Appl. Catal. B Environ.* **2022**, *311*, 121255. [[CrossRef](#)]
26. Qiu, Y.; Xing, Z.; Guo, M.; Li, Z.; Wang, N.; Zhou, W. Hollow cubic Cu_{2-x}S/Fe-POMs/AgVO₃ dual Z-scheme heterojunctions with wide-spectrum response and enhanced photothermal and photocatalytic-fenton performance. *Appl. Catal. B Environ.* **2021**, *298*, 120628. [[CrossRef](#)]
27. Zheng, D.; Cao, X.N.; Wang, X. Precise formation of a hollow carbon nitride structure with a janus surface to promote water splitting by photoredox catalysis. *Angew. Chem. Int. Ed.* **2016**, *55*, 11512–11516. [[CrossRef](#)]
28. Xu, Q.; Zhang, L.; Cheng, B.; Fan, J.; Yu, J. S-scheme heterojunction photocatalyst. *Chem* **2020**, *6*, 1543–1559. [[CrossRef](#)]
29. Xiao, Y.; Yao, B.; Cao, M.; Wang, Y. Super-Photothermal Effect-Mediated Fast Reaction Kinetic in S-Scheme Organic/Inorganic Heterojunction Hollow Spheres Toward Optimized Photocatalytic Performance. *Small* **2023**, *19*, 2207499. [[CrossRef](#)]
30. Ruan, X.; Huang, C.; Cheng, H.; Zhang, Z.; Cui, Y.; Li, Z.; Xie, T.; Ba, K.; Zhang, H.; Zhang, L.; et al. A Twin S-Scheme Artificial Photosynthetic System with Self-Assembled Heterojunctions yields Superior Photocatalytic Hydrogen Evolution Rate. *Adv. Mater.* **2023**, *35*, 2209141. [[CrossRef](#)]
31. Le, S.; Zhu, C.; Cao, Y.; Wang, P.; Liu, Q.; Zhou, H.; Chen, C.; Wang, S.; Duan, S. V₂O₅ nanodot-decorated laminar C₃N₄ for sustainable photodegradation of amoxicillin under solar light. *Appl. Catal. B Environ.* **2022**, *303*, 120903. [[CrossRef](#)]

32. Cheng, C.; He, B.; Fan, J.; Cheng, B.; Cao, S.; Yu, J. An inorganic/organic S-scheme heterojunction H₂-production photocatalyst and its charge transfer mechanism. *Adv. Mater.* **2021**, *33*, 2100317. [[CrossRef](#)] [[PubMed](#)]
33. Jia, X.; Hu, C.; Sun, H.; Cao, J.; Lin, H.; Li, X.; Chen, S. A dual defect co-modified S-scheme heterojunction for boosting photocatalytic CO₂ reduction coupled with tetracycline oxidation. *Appl. Catal. B Environ.* **2023**, *324*, 122232. [[CrossRef](#)]
34. Zhang, X.; Kim, D.; Yan, J.; Lee, L.Y.S. Photocatalytic CO₂ reduction enabled by interfacial S-scheme heterojunction between ultrasmall copper phosphosulfide and g-C₃N₄. *ACS Appl. Mater. Interfaces* **2021**, *13*, 9762–9770. [[CrossRef](#)]
35. Dai, Z.; Zhen, Y.; Sun, Y.; Li, L.; Ding, D. ZnFe₂O₄/g-C₃N₄ S-scheme photocatalyst with enhanced adsorption and photocatalytic activity for uranium (VI) removal. *Chem. Eng. J.* **2021**, *415*, 129002. [[CrossRef](#)]
36. Khan, A.A.; Tahir, M.; Mohamed, A.R. Constructing S-scheme heterojunction of carbon nitride nanorods (g-CNR) assisted trimetallic CoAlLa LDH nanosheets with electron and holes moderation for boosting photocatalytic CO₂ reduction under solar energy. *Chem. Eng. J.* **2022**, *433*, 133693. [[CrossRef](#)]
37. Wang, J.; Wang, G.; Cheng, B.; Yu, J.; Fan, J. Sulfur-doped g-C₃N₄/TiO₂ S-scheme heterojunction photocatalyst for Congo Red photodegradation. *Chin. J. Catal.* **2021**, *42*, 56–68. [[CrossRef](#)]
38. Babu, B.; Shim, J.; Kadam, A.N.; Yoo, K. Modification of porous g-C₃N₄ nanosheets for enhanced photocatalytic activity: In-situ synthesis and optimization of NH₄Cl quantity. *Catal. Commun.* **2019**, *124*, 123–127. [[CrossRef](#)]
39. Chen, K.; Shi, Y.; Shu, P.; Luo, Z.; Shi, W.; Guo, F. Construction of core-shell FeS₂@ZnIn₂S₄ hollow hierarchical structure S-scheme heterojunction for boosted photothermal-assisted photocatalytic H₂ production. *Chem. Eng. J.* **2023**, *454*, 140053. [[CrossRef](#)]
40. Suzuki, V.Y.; Amorin, L.H.C.; Fabris, G.S.L.; Dey, S.; Sambrano, J.R.; Cohen, H.; Oron, D.; Porta, F.A.L. Enhanced Photocatalytic and Photoluminescence Properties Resulting from Type-I Band Alignment in the Zn₂GeO₄/g-C₃N₄ Nanocomposites. *Catalysts* **2022**, *12*, 692. [[CrossRef](#)]
41. Babu, B.; Shim, J.; Yoo, K. Efficient solar-light-driven photoelectrochemical water oxidation of one-step in-situ synthesized Co-doped g-C₃N₄ nanolayers. *Ceram. Int.* **2020**, *46*, 16422–16430. [[CrossRef](#)]
42. Guo, M.; Zhao, T.; Xing, Z.; Qiu, Y.; Pan, K.; Li, Z.; Yang, S.; Zhou, W. Hollow Octahedral Cu_{2-x}S/CdS/Bi₂S₃ p-n-p Type Tandem Heterojunctions for Efficient Photothermal Effect and Robust Visible-Light-Driven Photocatalytic Performance. *ACS Appl. Mater. Interfaces* **2020**, *12*, 40328–40338. [[CrossRef](#)] [[PubMed](#)]
43. Li, X.; Kang, B.; Dong, F.; Zhang, Z.; Luo, X.; Han, L.; Huang, J.; Feng, Z.; Chen, Z.; Xu, J.; et al. Enhanced photocatalytic degradation and H₂/H₂O₂ production performance of S-pCN/WO_{2.72} S-scheme heterojunction with appropriate surface oxygen vacancies. *Nano Energy* **2021**, *81*, 105671. [[CrossRef](#)]
44. Zhang, L.; Zhang, J.; Yu, H.; Yu, J. Emerging S-scheme photocatalyst. *Adv. Mater.* **2022**, *34*, 2107668. [[CrossRef](#)] [[PubMed](#)]
45. Moon, H.S.; Hsiao, K.C.; Wu, M.C.; Yun, Y.; Hsu, Y.J.; Yong, K. Spatial Separation of Cocatalysts on Z-Scheme Organic/Inorganic Heterostructure Hollow Spheres for Enhanced Photocatalytic H₂ Evolution and in-Depth Analysis of the Charge-Transfer Mechanism. *Adv. Mater.* **2023**, *35*, 2200172. [[CrossRef](#)] [[PubMed](#)]
46. Zhao, D.; Wang, Y.; Dong, C.L.; Huang, Y.C.; Chen, J.; Xue, F.; Shen, S.; Guo, L. Boron-doped nitrogen-deficient carbon nitride-based Z-scheme heterostructures for photocatalytic overall water splitting. *Nat. Energy* **2021**, *6*, 388–397. [[CrossRef](#)]
47. Wang, L.; Cheng, B.; Zhang, L.; Yu, J. In situ irradiated XPS investigation on S-scheme TiO₂@ZnIn₂S₄ photocatalyst for efficient photocatalytic CO₂ reduction. *Small* **2021**, *17*, 2103447. [[CrossRef](#)] [[PubMed](#)]
48. Chen, K.; Wang, X.; Li, Q.; Feng, Y.N.; Chen, F.F.; Yu, Y. Spatial distribution of ZnIn₂S₄ nanosheets on g-C₃N₄ microtubes promotes photocatalytic CO₂ reduction. *Chem. Eng. J.* **2021**, *418*, 129476. [[CrossRef](#)]
49. Li, X.; Tu, D.; Yu, S.; Song, X.; Lian, W.; Wei, J.; Shang, X.; Li, R.; Chen, Y. Highly efficient luminescent I-III-VI semiconductor nanoprobe based on template-synthesized CuInS₂ nanocrystals. *Nano Res.* **2019**, *12*, 1804–1809. [[CrossRef](#)]
50. Cheng, C.; Zhang, J.; Zhu, B.; Liang, G.; Zhang, L.; Yu, J. Verifying the Charge-Transfer Mechanism in S-Scheme Heterojunctions Using Femtosecond Transient Absorption Spectroscopy. *Angew. Chem. Int. Ed.* **2023**, *135*, e202218688. [[CrossRef](#)]
51. Jiang, X.; Huang, J.; Bi, Z.; Ni, W.; Gurzadyan, G.; Zhu, Y.; Zhang, Z. Plasmonic Active “Hot Spots”-Confined Photocatalytic CO₂ Reduction with High Selectivity for CH₄ Production. *Adv. Mater.* **2022**, *34*, 2109330. [[CrossRef](#)] [[PubMed](#)]
52. Wang, K.; Xing, Z.; Du, M.; Zhang, S.; Li, Z.; Pan, K.; Zhou, Z. Hollow MoSe₂@Bi₂S₃/CdS core-shell nanostructure as dual Z-scheme heterojunctions with enhanced full spectrum photocatalytic-photothermal performance. *Appl. Catal. B Environ.* **2021**, *281*, 119482. [[CrossRef](#)]
53. Zhang, H.C.; Kang, Z.X.; Han, J.J.; Wang, P.; Fan, J.T.; Shen, G.P. Photothermal nanoconfinement reactor: Boosting chemical reactivity with locally high temperature in a confined space. *Angew. Chem. Int. Ed.* **2022**, *134*, e202200093.
54. Xiao, Y.; Wang, K.; Yang, Z.; Xing, Z.; Li, Z.; Pan, K.; Zhou, W. Plasma Cu-decorated TiO_{2-x}/CoP particle-level hierarchical heterojunctions with enhanced photocatalytic-photothermal performance. *J. Hazard. Mater.* **2021**, *414*, 125487. [[CrossRef](#)]
55. Babu, B.; Koutavarapu, R.; Shim, J.; Yoo, K. Enhanced visible-light-driven photoelectrochemical and photocatalytic performance of Au-SnO₂ quantum dot-anchored g-C₃N₄ nanosheets. *Sep. Purif. Technol.* **2020**, *240*, 116652. [[CrossRef](#)]
56. Jiang, X.H.; Zhang, L.S.; Liu, H.Y.; Wu, D.S.; Wu, F.Y.; Tian, L.; Liu, L.L.; Zou, J.P.; Luo, S.L.; Chen, B.B. Silver single atom in carbon nitride catalyst for highly efficient photocatalytic hydrogen evolution. *Angew. Chem. Int. Ed.* **2020**, *132*, 23312–23316. [[CrossRef](#)]
57. Wang, X.; Wang, X.; Huang, J.; Li, S.; Meng, A.; Li, Z. Interfacial chemical bond and internal electric field modulated Z-scheme Sv-ZnIn₂S₄/MoSe₂ photocatalyst for efficient hydrogen evolution. *Nat. Commun.* **2021**, *12*, 4112. [[CrossRef](#)]
58. Amorin, L.H.; Suzuki, V.Y.; de Paula, N.H.; Duarte, J.L.; da Silva, M.A.T.; Taftd, C.A.; Porta, F.A.L. Electronic, structural, optical, and photocatalytic properties of graphitic carbon nitride. *New J. Chem.* **2019**, *43*, 13647–13653. [[CrossRef](#)]

59. Zhang, Y.; Zhao, J.; Wang, H.; Xiao, B.; Zhang, W.; Zhao, X.; Lv, T.; Thangamuthu, M.; Zhang, J.; Guo, Y.; et al. Single-atom Cu anchored catalysts for photocatalytic renewable H₂ production with a quantum efficiency of 56%. *Nat. Commun.* **2022**, *13*, 58. [[CrossRef](#)]
60. Wang, G.; Huang, R.; Zhang, J.; Mao, J.; Wang, D.; Li, Y. Synergistic Modulation of the Separation of Photo-Generated Carriers via Engineering of Dual Atomic Sites for Promoting Photocatalytic Performance. *Adv. Mater.* **2021**, *33*, 2105904. [[CrossRef](#)]
61. Xia, P.; Cao, S.; Zhu, B.; Liu, M.; Shi, M.; Yu, J.; Zhang, Y. Designing a 0D/2D S-scheme heterojunction over polymeric carbon nitride for visible-light photocatalytic inactivation of bacteria. *Angew. Chem. Int. Ed.* **2020**, *59*, 5218–5225. [[CrossRef](#)] [[PubMed](#)]
62. Zhao, T.; Xing, Z.; Xiu, Z.; Li, Z.; Yang, S.; Zhou, W. Oxygen-doped MoS₂ nanospheres/CdS quantum dots/g-C₃N₄ nanosheets super-architectures for prolonged charge lifetime and enhanced visible-light-driven photocatalytic performance. *ACS Appl. Mater. Interfaces* **2019**, *11*, 7104–7111. [[CrossRef](#)] [[PubMed](#)]
63. Zhang, G.; Xu, Y.; Yan, D.; He, C.; Li, Y.; Ren, X.; Zhang, P.; Mi, H. Construction of k⁺ ion gradient in crystalline carbon nitride to accelerate exciton dissociation and charge separation for visible light H₂ production. *ACS Catal.* **2021**, *11*, 6995–7005. [[CrossRef](#)]
64. She, P.; Qin, J.; Sheng, J.; Qi, Y.; Rui, H.; Zhang, W.; Ge, X.; Lu, G.; Song, X.; Rao, H. Dual-functional photocatalysis for cooperative hydrogen evolution and benzylamine oxidation coupling over sandwiched-like Pd@TiO₂@ZnIn₂S₄ nanobox. *Small* **2022**, *18*, 2015114. [[CrossRef](#)]
65. Jiménez-Calvo, P.; Caps, V.; Ghazzal, M.N.; Colbeau-Justin, C.; Keller, V. Au/TiO₂ (P25)-gC₃N₄ composites with low gC₃N₄ content enhance TiO₂ sensitization for remarkable H₂ production from water under visible-light irradiation. *Nano Energy* **2020**, *75*, 104888. [[CrossRef](#)]
66. Huang, W.X.; Li, Z.P.; Wu, C.; Zhang, H.J.; Sun, J.; Li, Q. Delaminating Ti₃C₂ MXene by blossom of ZnIn₂S₄ microflowers for noble-metal-free photocatalytic hydrogen production. *J. Mater. Sci. Technol.* **2022**, *120*, 89–98. [[CrossRef](#)]
67. Sun, M.; Zhou, Y.L.; Yu, T.; Wang, J. Synthesis of g-C₃N₄/WO₃-carbon microsphere composites for photocatalytic hydrogen production. *Int. J. Hydrog. Energy* **2022**, *47*, 10261–10276. [[CrossRef](#)]
68. Pan, J.Q.; Dong, Z.J.; Wang, B.B.; Jiang, Z.Y.; Zhao, C.; Wang, J.J.; Song, C.S.; Zheng, Y.Y.; Li, C.R. The enhancement of photocatalytic hydrogen production via Ti₃₊ self-doping black TiO₂/g-C₃N₄ hollow core-shell nano-heterojunction. *Appl. Catal. B Environ.* **2019**, *242*, 92–99. [[CrossRef](#)]

Disclaimer/Publisher's Note: The statements, opinions and data contained in all publications are solely those of the individual author(s) and contributor(s) and not of MDPI and/or the editor(s). MDPI and/or the editor(s) disclaim responsibility for any injury to people or property resulting from any ideas, methods, instructions or products referred to in the content.